RSC Advances

PAPER

View Article Online
View Journal | View Issue

Cite this: *RSC Adv.*, 2020, **10**, 12469

Perfect cubic La-doped boron clusters La_6&$[La@B_{24}]^{+/0}$ as the embryos of low-dimensional lanthanide boride nanomaterials†

Xiao-Qin Lu, Mei-Zhen Ao, Xin-Xin Tian, Wen-Yan Zan,* Yue-Wen Mu* and Si-Dian Li*

Received 19th February 2020
Accepted 16th March 2020

DOI: 10.1039/d0ra01616k

rsc.li/rsc-advances

La-doped boron nanoclusters have received considerable attention due to their unique structures and bonding. Inspired by recent experimental observations of the inverse sandwich D_{8h} La_2B_8 (**1**) and triple-decker C_{2v} $La_3B_{14}^-$ (**2**) and based on extensive global searches and first-principles theory investigations, we present herein the possibility of the perfect cubic La-doped boron clusters O_h La_6&$[La@B_{24}]^+$ (**3**, $^1A_{1g}$) and O_h La_6&$[La@B_{24}]$ (**4**, $^2A_{2g}$) which appear to be the embryos of the metallic one-dimensional $La_{10}B_{32}$ (**5**) nanowire, two-dimensional La_3B_{10} (**6**) nanosheet, and three-dimensional LaB_6 (**7**) nanocrystal, facilitating a bottom-up approach to build cubic lanthanide boride nanostructures from gas-phase clusters. Detailed molecular orbital and bonding analyses indicate that effective (d–p)σ, (d–p)π and (d–p)δ covalent coordination interactions exist in La_6&$[La@B_{24}]^{+/0}$ (**3**/**4**) clusters, while the 1D $La_{10}B_{32}$ (**5**), 2D La_3B_{10} (**6**), and 3D LaB_6 (**7**) crystals exhibit mainly electrostatic interactions between the trivalent La centers and cubic B_{24} frameworks, with weak but discernible coordination contributions from La (5d) ← B (2p) back-donations. The IR and Raman spectra of La_6&$[La@B_{24}]^{+/0}$ (**3**/**4**) and band structures of $La_{10}B_{32}$ (**5**) and La_3B_{10} (**6**) are computationally simulated to facilitate their future characterizations.

1. Introduction

As a prototypical electron-deficient element next to carbon in the periodical table, boron has a rich chemistry characterized with delocalized multicenter-two-electron (mc-2e) bonds in both bulk allotropes and polyhedral molecules.[1] Boron-based materials have found wide applications in field emissions, supercapacitors, optical absorptions, photodetectors, and *etc.*[2–6] A bottom-up approach has received considerable attention in the past two decades to investigate the structural transitions from small boron nanoclusters to boron nanomaterials. Persistent joint photoelectron spectroscopy (PES) and first-principles theory investigations in the past two decades by Wang and coworkers have unveiled an unexpectedly rich landscape for size-selected boron clusters from planar or quasi-planar $B_n^{-/0}$ (n = 3–38, 41 and 42) to cage-like borospherenes D_{2d} $B_{40}^{-/0}$ and C_3/C_2 B_{39}^-. Multiple low-lying isomers appear to compete and coexist in most gas-phase boron $B_n^{-/0}$ clusters, starting from n = 7.[7–10] Ion-mobility measurements in combination with density functional theory (DFT) calculations, on the other hand, have shown that boron cluster monocations (B_n^+) possess double-ring tubular structures in the size range between n = 16–25,[11] unveiling another structural domain for boron nanoclusters. Transition-metal-doping has proven to induce dramatic structural and bonding pattern changes to boron clusters. Typical examples include the transition-metal-centered monocyclic boron wheel clusters $M@B_n$ ($Co@B_8^-$, $Ru@B_9^-$, and $Ta@B_{10}^-$) with the maximum planar coordination number of CN = 10 and transition-metal-centered boron double-ring tubular clusters $M@B_n^-$ ($Co@B_{16}^-$, $Rh@B_{18}^-$, and $Ta@B_{20}^-$) with the record tubular coordination number of CN = 20 known in experiments.[12–18] A family of inverse sandwich di-lanthanide boron complexes D_{7h} $La_2B_7^-$, D_{8h} La_2B_8 (**1**), and D_{9h} $La_2B_9^-$ with a perfect B_n ring (n = 7, 8, 9) sandwiched between two La atoms were observed in 2018 in PES measurements.[19,20] The first inverse triple-decker di-lanthanide boron cluster C_{2v} $La_3B_{14}^-$ (**2**) was discovered in 2019 in a joint experimental and theoretical investigation[21] in which two conjoined La_2B_8 (**1**) inverse sandwiches share a B–B edge and a La vertex in the titled La–B_8–La–B_8–La motif. Boron clusters as typical Wankel motor molecules with fluxional bonds also exhibit structural fluxionalities where metal dopants play an important role.[22–25] Our group very recently predicted the possibility of the inverse sandwich double-ring tubular molecular rotor C_{2h} La_2&$[B_2@B_{18}]$ which possesses the smallest core–shell structure reported in boron clusters.[26]

Bulk lanthanide hexaboride LaB_6 (**7**) has been widely used as cathode materials due to its numerous excellent properties such as low work function, ultrahigh hardness, high chemical

Nanocluster Laboratory, Institute of Molecular Science, Shanxi University, Taiyuan 030006, China. E-mail: zanwy@sxu.edu.cn; ywmu@sxu.edu.cn; lisidian@sxu.edu.cn

† Electronic supplementary information (ESI) available. See DOI: 10.1039/d0ra01616k

inertness, and high melting point.[27–30] It possesses a typical cubic CaB_6-type lattice ($Pm\bar{3}m$, O_h^1) characterized with a 3D network constituted of B_6 octahedrons, with the interstitial locations filled by trivalent La atoms.[31] Interestingly, each unit cell in LaB_6 (7) contains a B_{24} cubic framework which possesses six equivalent B_8 rings on the surface sharing twelve B–B dumb-bells on the edges, with each B_8 ring sandwiched between two neighboring La atoms. The strong structural similarity between the gas-phase inverse sandwich La_2B_8 (**1**) complex and cubic three-dimensional (3D) LaB_6 (7) crystal has been previously noticed.[31] LaB_6 nanowires in cubic LaB_6 (7) lattice were also recently confirmed to be active electrochemical materials for supercapacitors.[32] However, a cubic embryo of the LaB_6 (7) lattice still remains unknown to date in a bottom-up approach starting from gas-phase clusters. Such a cubic embryo may also be used to form one-dimensional (1D) lanthanide boride nanowires and two-dimensional (2D) lanthanide boride nanosheets.

Keep the inspiration in mind and based on extensive global minimum (GM) searches and first-principles theory calculations, we predict herein the highly stable perfect cubic La-doped boron clusters O_h La_6&$[La@B_{24}]^+$ (**3**, $^1A_{1g}$) and O_h La_6&$[La@B_{24}]$ (**4**, $^2A_{2g}$) which consist of six equivalent La_2B_8 (**1**) inverse sandwiches embedded in a cube sharing one La atom at center. More interestingly, La_6&$[La@B_{24}]^{+/0}$ (**3**/**4**) clusters with a B_{24} framework turn out to be the cubic embryos of the metallic 1D $La_{10}B_{32}$ (**5**) nanowire, 2D La_3B_{10} (**6**) nanosheet, and 3D LaB_6 (7) nanocrystal in a bottom-up approach. The newly obtained ferromagnetic 1D $La_{10}B_{32}$ (**5**) and nonmagnetic 2D La_3B_{10} (**6**) are expected to serve as efficient electronical and optical nanomaterials.

2. Theoretical procedure

Extensive GM searches were performed on $La_7B_{24}^+$ monocation using the TGmin2 code[33] at the DFT level, in combination with manual structural constructions based on the experimentally observed La_2B_8 (**1**) and $La_3B_{14}^-$ (**2**). Over 3000 trial structures were explored in both singlet and triplet states at PBE/TZVP. The low-lying isomers were then fully optimized at the PBE0 (ref. 34) and TPSSh[35] levels with the 6-311+G* basis set[36] for B and Stuttgart relativistic small-core pseudopotential for La[37,38] using the Gaussian 09 program suite.[39] Low-lying isomers of the open-shell neutral La_7B_{24} were obtained from the corresponding lowest-lying structures of $La_7B_{24}^+$.

The GM search on 1D $La_{10}B_{32}$ (**5**) was performed with the EOU program developed by our group.[40] A GM search based on the PSO technique implemented in the widely used Particle Swarm Optimization (CALYPSO)[41] package was executed for 2D La_3B_{10} (**6**). The calculations on 1D $La_{10}B_{32}$ (**5**), 2D La_3B_{10} (**6**), and 3D LaB_6 (7) nanostructures were performed using the Vienna *ab initio* simulation package (VASP),[42,43] within the framework of projector augmented wave (PAW) pseudopotential method[44,45] and PBE generalized gradient approximation (GGA).[46,47] The Coulomb-corrected local spin-density approximation (LSDA+U) was utilized for both structural relaxation and static calculation ($U = 5$ eV).[31,48] The cutoff energy of the plane wave basis is set to 500 eV. Atomic structures are fully relaxed using the conjugate gradient method until the maximum force on each atom was less than 0.01 eV $Å^{-1}$ and the energy precision was set to 10^{-5} eV. Chemical bonding analyses were performed for La_6&$[La@B_{24}]^+$ (**3**) using the adaptive natural density partitioning (AdNDP) approach at the PBE0 level[49,50] and for 3D LaB_6 (7) crystal utilizing the solid-state AdNDP (SSAdNDP) method.[51,52] Natural bonding orbital (NBO) analyses were performed on $La_7B_{24}^+$ (**3**) using the NBO 6.0 program.[53] Born–Oppenheimer molecular dynamics (BOMD) simulations were performed on $La_7B_{24}^+$ (**3**) for 30 ps at 300 K and 1000 K using the CP2K software package.[54]

3. Results and discussions

3.1 Structures and stabilities

Starting from the experimentally observed C_{2v} $La_3B_{14}^-$ (**2**) which possesses a tilted La–B_8–La–B_8–La inverse triple-decker structure with two conjoined B_8 rings sharing a B–B dumb-bell, we manually constructed the perfect cubic hepta-lanthanide-doped boron clusters O_h La_6&$[La@B_{24}]^+$ (**3**, $^1A_{1g}$) and O_h La_6&$[La@B_{24}]$ (**4**, $^2A_{2g}$) from two C_{2v} $La_3B_{14}^-$ (**2**) clusters which share two B–B dumb-bells on the edges and one La atom at the center, with two extra La atoms added on the top and bottom, respectively. With one La atom endohedrally coordinated at the center (@) and six La atoms exohedrally coordinated on the surface (&), O_h La_6&$[La@B_{24}]^{+/0}$ (**3**/**4**) can be viewed as consisting of six equivalent La_2B_8 (**1**) inverse sandwiches embedded in a cube sharing twelve B–B dumb-bells on the edges and one La vertex at the center. Interestingly and encouragingly, as shown in Fig. S1 and S2,† extensive GM searches strongly suggest that the highly stable perfect cubic La_6&$[La@B_{24}]^+$ (**3**) and La_6&$[La@B_{24}]$ (**4**) with a B_{24} framework be the well-defined GMs of the systems with the lowest vibrational frequencies of 111 cm^{-1} and 112 cm^{-1}, respectively. La_6&$[La@B_{24}]^{+/0}$ (**3**/**4**) possess the optimized La–B distances of $r_{La-B} = 2.94/2.95$ Å between the central La atom and its cubic B_{24} ligand and $r'_{La-B} = 2.70/2.69$Å between the surface La atoms and their neighboring B_8 ligands on the surface, with the B–B distances of $r_{B-B} = 1.67/1.67$ Å within the B–B dumb-bells on the edges and $r'_{B-B} = 1.64/1.65$Å within the B_3 triangles at the corners. The large HOMO–LUMO gap of $\Delta E_{gap} = 2.35$ eV calculated for La_6&$[La@B_{24}]^+$ (**3**) well supports its high chemical stability. As shown in Fig. S1,† its second lowest-lying triplet C_1 La_6&$[La@B_{24}]^+$ (^3A) which is slightly distorted (with r_{La-B} = 2.93–2.95 Å and $r'_{La-B} = 2.70/2.71$Å) due to Jahn–Teller effect lies 1.30 and 1.36 eV higher than the O_h GM in energy at PBE0 and TPSSH levels, respectively. Both the distorted cubic quintet and heptet isomers with the relative energies of 2.50 eV and 3.53 eV at PBE0, respectively, appear to be much less stable (Fig. S1†). Extensive molecular dynamics simulations indicate that La_6&$[La@B_{24}]^+$ (**3**) is also highly dynamically stable, with the calculated average root-mean-square-deviations of RMSD = 0.12 Å and maximum bond length deviations of MAXD = 0.38 Å at 1000 K. Similar situation exists in La_6&$[La@B_{24}]$ (**4**). La_6&$[La@B_{24}]^{+/0}$ (**3**/**4**) are therefore the well-defined deep-lying GMs

of the systems highly stable both thermodynamically and dynamically.

We initially constructed a 1D La_5B_{16} nanowire ($P4/mmm$) (Fig. S3†) by extending the finite $La_6\&[La@B_{24}]^{+/0}$ (**3**/**4**) clusters periodically in one direction (x), resulting in a 1D nanowire with one small imaginary phonon frequency at 49i cm^{-1}. This imaginary phonon frequency corresponds to a typical Peierls phase transition which leads to the slightly more stable 1D $La_{10}B_{32}$ nanowire (**5**, $P4/mmm$) (by 0.07 eV) when the unit cell is doubled in size, with the two La atoms inside slightly off-centered by 0.22 Å (Fig. 1). Similarly, 2D La_3B_{10} (**6**) ($P4/mmm$) and 3D LaB_6 (**7**) ($Pm\bar{3}m$) networks can be obtained by expanding $La_6\&[La@B_{24}]^{+/0}$ (**3**/**4**) periodically in (x, y) and (x, y, z) directions, respectively (Fig. 1). The 1D (**5**), 2D (**6**), and 3D (**7**) networks possess the optimized lattice parameters of $a = 8.66$ Å, $a = b = 4.17$ Å and $a = b = c = 4.16$ Å at PBE level, respectively. Our calculated lattice parameters and La–B distance ($r_{La-B} = 3.06$ Å) for 3D LaB_6 (**7**) agree well with the corresponding experimentally measured values of $a = b = c = 4.16$ Å and $r_{La-B} = 3.05$ Å.[31] The newly obtained 2D La_3B_{10} (**6**) possesses the optimized La–B distances of $r_{La-B(x)} = r_{La-B(y)} = 3.05$ Å and $r_{La-B(z)} = 3.07$ Å between the central La atom and its B_{24} cubic ligand. Similar La–B distances exist in 1D $La_{10}B_{32}$ (**5**). These La–B distances turn out to be slightly longer than the corresponding La–B coordination bond lengths of $r_{La-B} = 2.94/2.95$ Å in $La_6\&[La@B_{24}]^{+/0}$ (**3**/**4**) clusters. Interestingly, as shown in Fig. S4 and S5,† 1D $La_{10}B_{32}$ (**5**) has the lowest cohesive energy among the 1D structures obtained *via* extensive EOU global searches, while La_3B_{10} (**6**) is the lowest-lying structure in all the 2D La_3B_{10} conformations probed by extensive PSO global searches, with the second lowest-lying 1D and 2D structures lying 3.13 eV and 1.88 eV higher in cohesive energy per unit cell than $La_{10}B_{32}$ (**5**) and La_3B_{10} (**6**), respectively. 1D $La_{10}B_{32}$ (**5**) and 2D La_3B_{10} (**6**) are thus strongly favored in thermodynamics compared with their other low-lying counterparts.

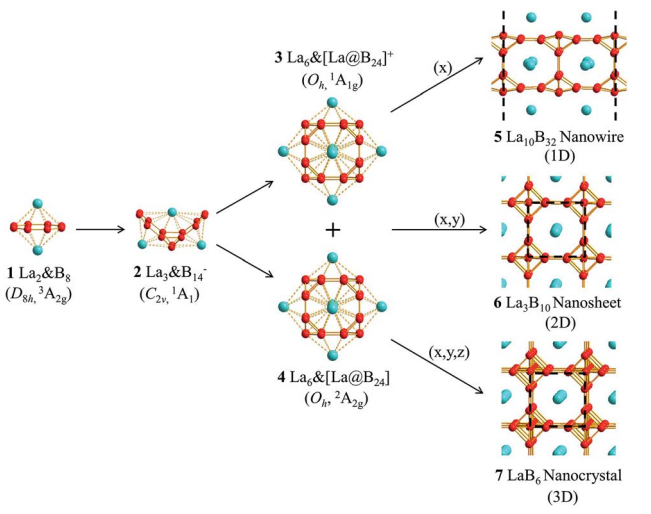

Fig. 1 Optimized structures of inverse sandwich D_{8h} $La_2\&B_8$ (**1**), inverse triple-decker C_{2v} $La_3@B_{14}^-$ (**2**), cubic O_h $La_6\&[La@B_{24}]^+$ (**3**), cubic O_h $La_6\&[La@B_{24}]$ (**4**), 1D $La_{10}B_{32}$ nanowire (**5**), 2D La_3B_{10} nanosheet (**6**), and 3D LaB_6 nanocrystal (**7**).

To evaluate the relative stability of 1D $La_{10}B_{32}$ (**5**), 2D La_3B_{10} (**6**), and 3D LaB_6 (**7**) networks, we computed their average cohesive energy per atom

$$E_{coh} = \frac{nE_{La} + mE_B - E_{La_nB_m}}{n+m}$$

where E_{La}, E_B, and $E_{La_nB_m}$ are the total energies of a single La atom, a single B atom, and a unit cell of the La_nB_m lattices and n and m are the numbers of La and B atoms, respectively. $La_{10}B_{32}$ (**5**), La_3B_{10} (**6**), and LaB_6 (**7**) appear to have the calculated cohesive energies of $E_{coh} = 6.33$, 6.50 and 6.95 eV per atom, respectively. These values appear to be systematically higher than the corresponding cohesive energy per atom of $E_{coh} = 5.65$ eV calculated for neutral embryo $La_6\&[La@B_{24}]$ (**4**).

3.2 Electronic structures and bonding patterns

The high stabilities of these cubic lanthanide boride nanostructures can be traced back to their unique electronic structures and bonding patterns. Detailed NBO analyses on closed-shell $La_6\&[La@B_{24}]^+$ (**3**) show that the central La atom possesses the natural atomic charge of $q_{La} = -0.50|e|$, electronic configuration of $La[Xe]4f^{0.18}5d^{3.04}6s^{0.24}$, and total Wiberg bond order of $WBI_{La} = 5.26$, while the six surface La atoms have the natural atomic charge of $q_{La} = +1.43|e|$, electronic configuration of $La[Xe]4f^{0.15}5d^{1.41}6s^{0.10}$, and total Wiberg bond order of $WBI_{La} = 2.86$. Obviously, both the central and surface La atoms in $La_6\&[La@B_{24}]^+$ (**3**) donate their $6s^2$ electrons almost completely to the B_{24} cubic ligand and there exists an effective La 5d ← B 2p back-donation from the cubic B_{24} ligand to the central La atom. Especially, the central La atom with the 5d occupation of $5d^{3.04}$ has a much higher total La–B coordination bond order (5.26) than that of the partially coordinated surface La atoms (2.86) with the 5d occupation of $5d^{1.41}$. Obvious La–B coordination interaction with the average La–B bond order of $WBI_{La-B} = 0.22$ exists between the central La and its 24 equivalent B ligands in $La_6\&[La@B_{24}]^+$ (**3**). The La coordination centers in inverse sandwich $La_2\&B_8$ (**1**) and $La_3@B_{14}^-$ (**2**) possess the net atomic charges of $q_{La} = +1.29$, $+1.39/1.17|e|$, electronic configurations of $La[Xe]4f^{0.17}5d^{1.49}6s^{0.10}$, $La[Xe]4f^{0.13/0.16}5d^{1.37/1.63}6s^{0.11/0.11}$, and total Wiberg bond orders of $WBI_{La} = 2.87$, 2.88/3.08, repectively, similar to the situation in the six surface La atoms in $La_6\&[La@B_{24}]^+$ (**3**). Detailed molecular orbital (MO) analyses indicate that all the occupied orbitals of the closed-shell $La_6\&[La@B_{24}]^+$ (**3**) are effective bonding MOs, while its lowest unoccupied MO (LUMO, (a_{2g})) is basically an anti-bonding orbital mainly originated from the 5d atomic orbitals of the six surface La atoms (Fig. S6†). With a valence electron occupying the non-degenerate LUMO (a_{2g}) of $La_6\&[La@B_{24}]^+$ (**3**), neutral $La_6\&[La@B_{24}]$ (**4**) possesses a singly occupied highest occupied MO (SOMO (a_{2g})). Such an electron occupation helps maintain the O_h symmetry of the open-shell neutral which possesses the same geometry as $La_6\&[La@B_{24}]^+$ (**3**).

To better understand the bonding nature and stabilization mechanism, we performed a detailed AdNDP bonding analysis on the closed-shell $La_6\&[La@B_{24}]^+$ (**3**) which recovers both the localized and delocalized bonds of the system. As clearly

indicated in Fig. 2a, $La_6\&[La@B_{24}]^+$ (**3**) possesses 12 equivalent 2c-2e B–B σ bonds on twelve B–B dumb-bells with the occupation number of ON = 1.78|*e*| and 8 equivalent 3c-2e σ bonds over eight B_3 triangles at the corners of the cube with ON = 1.83|*e*|, forming the σ-skeleton on the cubic B_{24} ligand. The remaining 26 delocalized bonds are mainly responsible for the La–B coordination interactions in the complex, including 6 10c-2e $B_8(\sigma)$–$La_2(d_\sigma)$ bonds, 12 10c-2e $B_8(\sigma)$–$La_2(d_\pi)$ bonds, and 6 10c-2e $B_8(\pi)$–$La_2(d_\delta)$ bonds with ON = 1.72–1.90|*e*| on six equivalent conjoined La_2B_8 (**1**) inverse sandwiches embedded in the cube and 2 31c-2e $B_{24}(\pi)$–$La_7(d_\sigma)$ bonds totally delocalized over the whole molecule with ON = 2.00|*e*| (Fig. 2a, see Fig. S7† for more details). Overall, cubic $La_6\&[La@B_{24}]^+$ (**3**) has similar (d–p)σ, (d–p)π, and (d–p)δ coordination interactions with that of observed inverse sandwich La_2B_8 (**1**) and triple-decker $La_3B_{14}^-$ (**2**).[19–21] The bonding pattern presented above provides further evidence that all the occupied MOs of $La_6\&[La@B_{24}]^+$ (**3**) are intrinsically bonding MOs (Fig. S6†), while all its antibonding MOs remain empty. Such a unique electron occupation renders an exceptionally high stability to the monocation.

We also performed a detailed SSAdNDP analysis on the periodical 3D LaB_6 (**7**) cubic lattice in Fig. 2b. There are 3 equivalent 2c-2e B–B σ bonds on three B–B dumb-bells in the cubic unit cell with ON = 1.80|*e*| which correspond to the 12 2c-2e B–B σ bonds on the B_{24} ligand in $La_6\&[La@B_{24}]^+$ (**3**). The remaining 8 equivalent 4c-2c $B_3(\sigma)$–$La(d_\sigma)$ bonds between the central La atom and the eight B_3 triangles at the corners with ON = 1.77|*e*| represent mainly electrostatic interactions between the trivalent La center and B_{24} cubic framework, with weak but discernible coordination contributions from La (5d) ← B (2p) back-donations (Fig. 2b). Similar bonding patterns exist in 1D $La_{10}B_{32}$ (**5**) and 2D La_3B_{10} (**6**). Detailed Bader charge analyses[55] indicate that the central La atom in LaB_6 (**7**) carries the net atomic charges of q_{La} = +1.71|*e*|, with its B neighbors possessing the average atomic charge of q_B = −0.29|*e*|. The formation of rare earth (RE) boride crystals REB_6 in infinite lattices involve an obvious electron transfer from the trivalent RE centers to the boron sublattice. 1D (**5**), 2D (**6**), and 3D (**7**) nanocrystals with the elongated La–B distances of $r_{La-B(z)}$ = 3.05–3.07 Å possess obviously weaker La–B covalent coordination interactions than that in $La_6\&[La@B_{24}]^{+/0}$ (**3**/**4**) clusters which have the La–B coordination distances of r_{La-B} = 2.94–2.95 Å. The size of the trivalent RE atoms, rather than their electron configuration, is the main factor responsible for their boride structures.[56]

The calculated band structures and corresponding projected density of states (PDOS) of 1D $La_{10}B_{32}$ (**5**) and 2D La_3B_{10} (**6**) nanostructures are depicted in Fig. 3. Notably, these nanostructures all appear to be metallic in nature. Both 2p orbitals from B atoms and 5d orbitals from La centers contribute to the calculated PDOS near the Fermi level, with La-5d orbitals making major contributions to the PDOS above the Fermi level, while B-2p orbitals dominating the PDOS below the Fermi level. Both spin unpolarized and spin-polarized computations were carried out to determine the ground states for these nanomaterials during the structural optimizations. 1D $La_{10}B_{32}$ (**5**) network turned out to be a ferromagnetic metal with the total magnetic moment of 2.03 μ_B per unit cell which mainly originates from the surface La atoms (with each surface La carrying the magnetic moment of 0.12 μ_B, while each central La carrying the magnetic moment of only 0.008 μ_B). In contrast, both 2D La_3B_{10} (**6**) and 3D LaB_6 (**7**) are nonmagnetic in nature with the calculated magnetic moments of zero.

3.3 Simulated IR and Raman spectra of the $La_6\&[La@B_{24}]^+$ embryo

Infrared photodissociation (IR-PD) in combination with first-principles theory calculations has proven to be a powerful means to characterize novel gas-phase clusters.[57,58] We computationally simulate the IR and Raman spectra of the closed-shell $La_6\&[La@B_{24}]^+$ (**3**) in Fig. 4a to facilitate its future experimental characterizations. The high-symmetry O_h $La_6\&[La@B_{24}]^+$

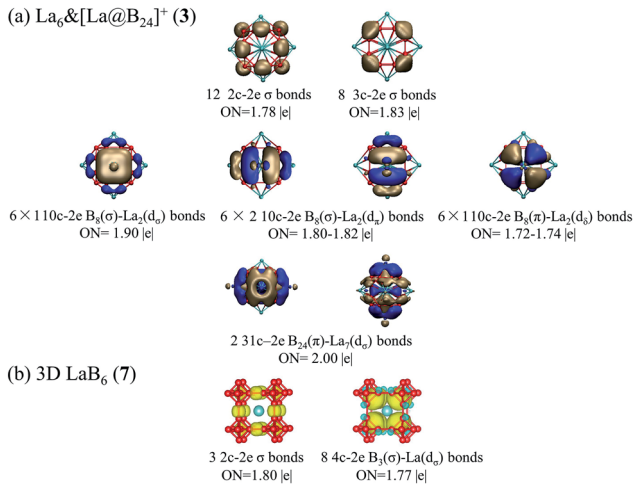

Fig. 2 AdNDP bonding patterns of (a) $La_6\&[La@B_{24}]^+$ (**3**) cluster and (b) 3D LaB_6 (**7**) crystal, with the occupation numbers (ONs) indicated. Each 10c-2e B_8–La_2 bond in the second row represents six equivalent La–B_8–La coordination bonds, as detailed in the ESI in Fig. S7.†

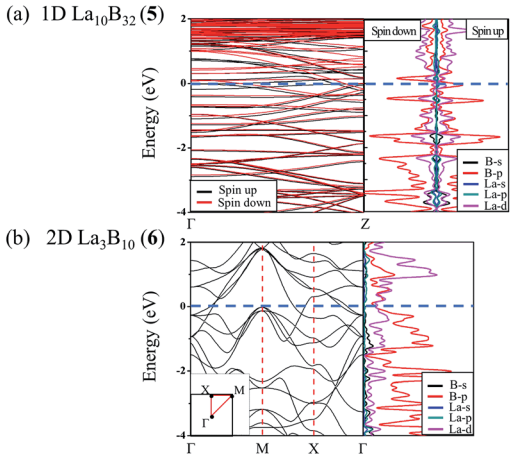

Fig. 3 Calculated band structures and projected densities of states (PDOS) of (a) 1D $La_{10}B_{32}$ (**5**) and (b) 2D La_3B_{10} (**6**) using the PBE functional.

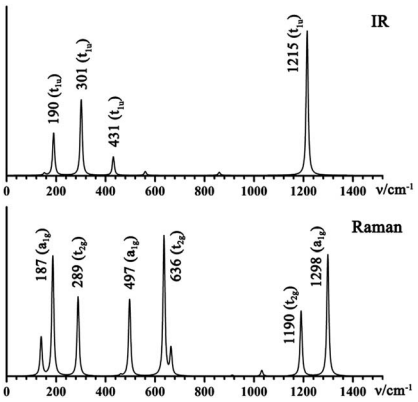

Fig. 4 Simulated IR and Raman spectra of O_h La_6&$[La@B_{24}]^+$ (**3**) at PBE0/6-311+G(d) level.

possesses relatively simple vibrational spectra, with sharp asymmetrical IR vibrations at 190 (t_{1u}), 301 (t_{1u}), 431 (t_{1u}), and 1215 (t_{1u}) cm^{-1} and symmetrical Raman features at 187 (a_{1g}), 289 (t_{2g}), 497 (a_{1g}), 636 (t_{2g}), 1190 (t_{2g}) and 1298 (a_{1g}) cm^{-1}, respectively. The strong Raman peaks at 187 cm^{-1} and 497 cm^{-1} mainly represent the typical radial breathing modes (RBMs) (a_{1g}) of the six evenly distributed surface La atoms and the B_{24} cubic framework, respectively. Such RBM spectral features can be used to characterize hollow boron structures.[59] As shown in Fig. S8,† similar but slightly more complicated IR and Raman spectra are obtained for the open-shell neutral La_6&$[La@B_{24}]$ (**4**).

4. Conclusions

Based on extensive GM searches and first-principles theory calculations, we have predicted in this work the highly stable perfect cubic O_h La_6&$[La@B_{24}]^{+/0}$ (**3**/**4**) which are the embryos of the metallic 1D $La_{10}B_{32}$ (**5**) nanowire, 2D La_3B_{10} (**6**) nanosheet, and 3D LaB_6 (**7**) nanocrystal, building a bridge between gas-phase lanthanide boride clusters and their low-dimensional nanomaterials. La_6&$[La@B_{24}]^{+/4}$ (**3**/**4**) clusters and 1D (**5**), 2D (**6**), and 3D (**7**) nanocrystals exhibit strong similarities in structures, with the periodical nanostructures possessing obviously weaker La (5d) ← B (2p) back-donations than their cubic embryos. Using the commercially available 3D LaB_6 (**7**) as target, it is possible to synthesize the newly predicted 0D (**3**/**4**), 1D (**5**), and 2D (**6**) nanomaterials by laser ablations, chemical vaporizations, or arc-discharges. The construction strategy demonstrated in this work may be applicable to the design of more rare-earth boride nanomaterials.

Conflicts of interest

There are no conflicts to declare.

Acknowledgements

The work was supported by the National Natural Science Foundation of China (21720102006 to S.-D. Li, 11504213 to Y.-W. Mu, and 21803037 to W.-Y. Zan).

Notes and references

1 F. A. Cotton, G. Wilkinson, C. A. Murrillo and M. Bochmann, *Advanced Inorganic Chemistry*, Wiley, New York, 6th edn, 1999.
2 J. Q. Xu, G. H. Hou, H. Q. Li, T. Y. Zhai, B. P. Dong, H. L. Yan, Y. R. Wang, B. H. Yu, Y. Bando and D. Golberg, *NPG Asia Mater.*, 2013, **5**, e53.
3 A. Sussardi, T. Tanaka, A. U. Khan, L. Schlapbach and T. Mori, *J. Materiomics*, 2015, **1**, 196.
4 G. Akopov, M. T. Yeung and R. B. Kaner, *Adv. Mater.*, 2017, **29**, 1604506.
5 S. Carenco, D. Portehault, C. Boissière, N. Mézailles and C. Sanchez, *Chem. Rev.*, 2013, **113**, 7981.
6 Y. Tian, Z. k. Guo, T. Zhang, H. J. Lin, Z. J. Li, J. Chen, S. Z. Deng and F. Liu, *Nanomaterials*, 2019, **9**, 538.
7 Q. Chen, W. L. Li, Y. F. Zhao, S. Y. Zhang, H. S. Hu, H. Bai, H. R. Li, W. J. Tian, H. G. Lu, H. J. Zhai, S. D. Li, J. Li and L. S. Wang, *ACS Nano*, 2015, **9**, 754.
8 H. J. Zhai, Y. F. Zhao, W. L. Li, Q. Chen, H. Bai, H. S. Hu, Z. A. Piazza, W. J. Tian, H. G. Lu, Y. B. Wu, Y. W. Mu, G. F. Wei, Z. P. Liu, J. Li, S. D. Li and L. S. Wang, *Nat. Chem.*, 2014, **6**, 727.
9 H. Bai, T. T. Chen, Q. Chen, X. Y. Zhao, Y. Y. Zhang, W. J. Chen, W. L. Li, L. F. Cheung, B. Bai, J. Cavanagh, W. Huang, S. D Li, J. Li and L. S. Wang, *Nanoscale*, 2019, **11**, 23286.
10 T. Jian, X. N. Chen, S. D. Li, A. I. Boldyrev, J. Li and L. S. Wang, *Chem. Soc. Rev.*, 2019, **48**, 3550.
11 E. Oger, N. R. M. Crawford, R. Kelting, P. Weis, M. M. Kappes and R. Ahlrichs, *Angew. Chem., Int. Ed.*, 2007, **46**, 8503.
12 W. L. Li, C. Romanescu, T. R. Galeev, Z. A. Piazza, A. I. Boldyrev and L. S. Wang, *J. Am. Chem. Soc.*, 2012, **134**, 165.
13 T. R. Galeev, C. Romanescu, W. L. Li, L. S. Wang and A. I. Boldyrev, *Angew. Chem., Int. Ed.*, 2012, **51**, 2101.
14 C. Romanescu, T. R. Galeev, W. L. Li, A. I. Boldyrev and L. S. Wang, *Acc. Chem. Res.*, 2013, **46**, 350.
15 I. A. Popov, T. Jian, G. V. Lopez, A. I. Boldyrev and L. S. Wang, *Nat. Commun.*, 2015, **6**, 8654.
16 T. Jian, W. L. Li, X. Chen, T. T. Chen, G. V. Lopez, J. Li and L. S. Wang, *Chem. Sci.*, 2016, **7**, 7020.
17 W. L. Li, T. Jian, X. Chen, H. R. Li, T. T. Chen, X. M. Luo, S. D. Li, J. Li and L. S. Wang, *Chem. Commun.*, 2017, **53**, 1587.
18 T. Heine and G. Merino, *Angew. Chem., Int. Ed.*, 2012, **51**, 4275.
19 W. L. Li, T. T. Chen, D. H. Xing, X. Chen, J. Li and L. S. Wang, *Proc. Natl. Acad. Sci. U. S. A.*, 2018, **115**, E6972.
20 T. T. Chen, W. L. Li, J. Li and L. S. Wang, *Chem. Sci.*, 2019, **10**, 2534.
21 T. T. Chen, W. L. Li, W. J. Chen, J. Li and L. S. Wang, *Chem. Commun.*, 2019, **55**, 7864.
22 S. Pan, J. Barroso, S. Jalife, T. Heine, K. R. Asmis and G. Merino, *Acc. Chem. Res.*, 2019, **52**, 2732.

23 L. Liu, D. Moreno, E. Osorio, A. C. Castro, S. Pan, P. K. Chattaraj, T. Heinea and G. Merino, *RSC Adv.*, 2016, **6**, 27177.
24 G. Martínez-Guajardo, J. L. Cabellos, A. Díaz-Celaya, S. Pan, R. Islas, P. K. Chattaraj, T. Heine and G. Merino, *Sci. Rep.*, 2015, **5**, 11287.
25 M. Yan, H. R. Li, X. Y. Zhao, X. Q. Lu, Y. W. Mu, H. G. Lu and S. D. Li, *J. Comput. Chem.*, 2019, **40**, 966.
26 X. Q. Lu, Q. Chen, X. X. Tian, Y. W. Mu, H. G. Lu and S. D. Li, *Nanoscale*, 2019, **11**, 21311.
27 C. H. Chen, T. Aizawa, N. Iyi, A. Sato and S. Otani, *J. Alloys Compd.*, 2004, **366**, L6.
28 H. Zhang, J. Tang, J. S. Yuan, J. Ma, N. Shinya, K. Nakajima, H. Murakami, T. Ohkubo and L. C. Qin, *Nano Lett.*, 2010, **10**, 3539.
29 S. S. Ordanyan, S. V. Vikhman, D. D. Nesmelov, D. P. Danilovich and I. B. Panteleev, *Adv. Sci. Technol.*, 2014, **89**, 47.
30 H. Zhang, J. Tang, L. Zhang, B. An and L. C. Qin, *Appl. Phys. Lett.*, 2008, **92**, 173121.
31 W. L. Li, C. Ertural, D. Bogdanovski, J. Li and R. Dronskowski, *Inorg. Chem.*, 2018, **57**, 12999.
32 Q. Xue, Y. Tian, S. Z. Deng, Y. Huang, M. S. Zhu, Z. X. Pei, H. F. Li, F. Liu and C. Y. Zhi, *Mater. Today Energy*, 2018, **10**, 28.
33 X. Chen, Y. F. Zhao, Y. Y. Zhang and J. Li, *J. Comput. Chem.*, 2019, **40**, 1105.
34 C. Adamo and V. Barone, *J. Chem. Phys.*, 1999, **110**, 6158.
35 J. Tao, J. P. Perdew, V. N. Staroverov and G. E. Scuseria, *Phys. Rev. Lett.*, 2003, **91**, 146401.
36 R. Krishnan, J. S. Binkley, R. Seeger and J. A. Pople, *J. Chem. Phys.*, 1980, **72**, 650.
37 D. Feller, *J. Comput. Chem.*, 1996, **17**, 1571.
38 L. Schuchardt, B. T. Didier, T. Elsethagen, L. Sun, V. Gurumoorthi, J. Chase, J. Li and T. L. Windus, *J. Chem. Inf. Model.*, 2007, **47**, 1045.
39 M. J. Frisch, *et al.*, *Gaussian 09, Revision D.01*, Gaussian Inc., Wallingford, CT, 2009.
40 F.-W. Mu, A global search code based on exhaustible operations of units, 2020, to be published.
41 Y. Wang, J. Lv, L. Zhu and Y. Ma, *Phys. Rev. B: Condens. Matter Mater. Phys.*, 2010, **82**, 094116.
42 G. Kresse and J. Furthmüller, *Comput. Mater. Sci.*, 1996, **6**, 15.
43 G. Kresse and J. Furthmüller, *Phys. Rev. B: Condens. Matter Mater. Phys.*, 1996, **54**, 11169.
44 P. E. Blöchl, *Phys. Rev. B: Condens. Matter Mater. Phys.*, 1994, **50**, 17953.
45 G. Kresse, *Phys. Rev. B: Condens. Matter Mater. Phys.*, 1999, **59**, 1758.
46 J. P. Perdew, K. Burke and M. Ernzerhof, *Phys. Rev. Lett.*, 1996, **77**, 3865.
47 J. P. Perdew, K. Burke and M. Ernzerhof, *Phys. Rev. Lett.*, 1997, **78**, 1396.
48 V. I. Anisimov, I. V. Solovyev, M. A. Korotin, M. T. Czyżyk and G. A Sawatzky, *Phys. Rev. B: Condens. Matter Mater. Phys.*, 1993, **48**, 16929.
49 N. V. Tkachenko and A. I. Boldyrev, *Phys. Chem. Chem. Phys.*, 2019, **21**, 9590.
50 T. Lu and F. W. Chen, *J. Comput. Chem.*, 2012, **33**, 580.
51 B. D. Dunnington and J. R. Schmidt, *J. Chem. Theory Comput.*, 2012, **8**, 1902.
52 T. R. Galeev, B. D. Dunnington, J. R. Schmidt and A. I. Boldyrev, *Phys. Chem. Chem. Phys.*, 2013, **15**, 5022.
53 P. E. D. Glendening, J. K. Badenhoop, A. E. Reed, J. E. Carpenter, J. A. Bohmann, C. M. Morales, C. R. Landis and F. Weinhold, *NBO 6.0*, 2013.
54 J. VandeVondele, M. Krack, F. Mohamed, M. Parrinello, T. Chassaing and J. Hutter, *Comput. Phys. Commun.*, 2005, **167**, 103.
55 G. Henkelman, A. Arnaldsson and H. Jonsson, *Comput. Mater. Sci.*, 2006, **36**, 354.
56 J. Etourneau and P. Hagenmuller, *Philos. Mag. B*, 1985, **52**, 589.
57 G. Wang, M. Zhou, J. T. Goettel, G. J. Schrobilgen, J. Su, J. Li, T. Schloder and S. Riedel, *Nature*, 2014, **514**, 475.
58 M. R. Fagiani, X. W. Song, P. Petkov, S. Debnath, S. Gewinner, W. Schcllkopf, T. Heine, A. Fielicke and K. R. Asmis, *Angew. Chem., Int. Ed.*, 2016, **56**, 501.
59 D. Ciuparu, R. F. Klie, Y. M. Zhu and L. Pfefferle, *J. Phys. Chem. B*, 2004, **108**, 39.